

Advances in particle size analysis with transmitted light techniques

D. Wirz, H.-J. Bart

Thermische Verfahrenstechnik, TU Kaiserslautern, Germany

Received October 4, 2020; Revised November 2, 2020

Particle size distributions (PSD) play a key role in many multiphase processes, but a quantitative analysis is a challenging task, especially due to a lack of reliable measurement techniques. The Optical Multimode Online Probe (OMOP) for droplet size analysis based on a shadowgraphic transmitted light approach was further developed for bubbles or solids in liquids or even droplets in sprays. A key problem for laboratory scale measurement techniques are industrial processes conditions like elevated temperature and pressure. This article gives an overview on the developments, for example with a bubble column where pressures up to 5 bar influence the bubble size, a crystallizer where the transient PSD can be a direct property of the product and a stirred pump-mixer-settler where the pumping behavior and impeller design has a direct effect of the droplet size.

Keywords: shadowgraphic probe, particle size distribution, telecentric principle, liquid-liquid, solid-liquid, gas-liquid

INTRODUCTION

Multiphase flows dominate a vast majority of processes in chemical and process industry, while the particulate phase can either be a fluid or a solid and the continuous phase can either be gaseous or liquid. The particulate properties of the disperse phase have an important effect on (reactive) mass transfer, particulate growth, aggregation and breakup. Therefore, the particulate state is important for the performance of a process and the product quality and yield or any product property (size, shape, etc.).

A review on measurement of the PSD is given elsewhere [1, 2] but the majority of measurement techniques uses optical techniques based on laser light or imaging techniques, the latter with the use of a digital camera. Commercial incident light techniques are offered by Mettler Toledo Inc. [3], SOPAT GmbH [4] and Pixact Ltd [5] and as laser-optical probe, the Focus Beam Reflectance Measurement [6], by Mettler Toledo Inc. In this article an alternative shadowgraphic setup with telecentric lenses instead of an incident light technique will be discussed in detail in the following.

Telecentric shadowgraphic technique

A new telecentric shadowgraphic setup was reported in 2013 for the measurement of droplet size distribution (DSD) in extraction columns [7, 8] and is called the Optical Multimode Online Probe (OMOP) [9]. This first version is executed as a flange that is placed between the glass compartments in laboratory scale, as depicted in Fig. 1. The measurement flange consists of two tubes with protection windows in the front that are

diametrically inserted in the flange. The tubes are adjustable and provide a flexible measurement volume and position. The LED illumination unit emits a parallel light bundle through a plano-convex lens. The camera with the telecentric lens is positioned in the opposite site and captures the images. The tubes are sealed *via* dynamic sealings and can therefore be adjusted during the process and positioned *via* a fixing screw. This setup delivers pictures with a high contrast between the particles (dark) and the background (bright), examples are given later in Figs. 5, 8 and 12.

In addition, the telecentric lens has a distance-independent magnification (telecentric principle), therefore the shadowgraphic projection of captured particle size is not influenced by their distance to the lens [10]. This is a common drawback with endocentric lenses that are used in commercially available probes, requiring accurate calibration and advanced image algorithm that deals with the distortion in size and blurriness [11, 12]. In addition, telecentric lenses provide high accuracy of 8.2% for droplets down to 8 μm [13]. In addition, telecentric lenses provide higher depth of fields [10] resulting in a better image quality allowing to detect more particles, which are easier to evaluate with image processing tools.

The main advantage of endoscopic probes is their easy integration, as they are inserted in any apparatus *via* a nozzle-spout. Two endoscopic probes (see Fig. 2) were built in the recent years to overcome the drawback of tedious flange integration when using one-sided access. These probes integrate all features of the telecentric shadowgraphic principle and are less invasive and can be designed in any dimension (even as a small laboratory probe [14]) and are

* To whom all correspondence should be sent:

E-mail: dominic.wirz@mv.uni-kl.de

completely inline adjustable in terms of depth of field, measurement volume and illumination. Their integration into different processes will be discussed with different case studies.

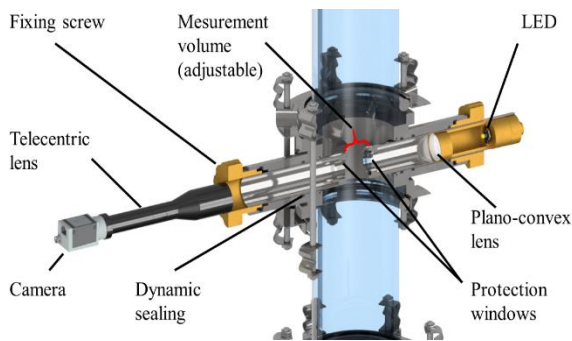


Figure 1. Cut through a DN100 shadowgraphic measurement flange.

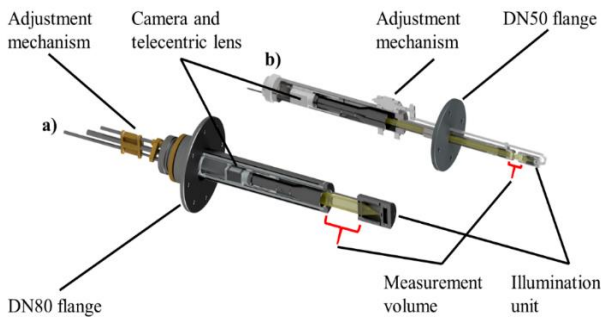


Figure 2. Endoscopic shadowgraphic probes in a) DN80; b) DN50.

Case Studies

Bubble Column

Bubble size distributions (BSD) markedly influence gas-liquid mass transfer area [15] and little is reported besides integral gas holdup for industrial relevant processes. Studies of the BSD are commonly found in lab-scale rectangular bubble columns [16–19] but investigations in closed systems or at industrial relevant conditions are rarely found. In order to demonstrate the applicability of the shadowgraphic principle a semi-batch bubble column with a special measurement flange (see Fig. 3) is built for process conditions up to 100 bar and 650K, with a height of 2100 mm and a perforated plate gas distributor ($97 \times 700 \mu\text{m}$ holes in 10 mm distance). The measurement flange is 860 mm above the gas distributor which is delivering in-house pressured air controlled by a mass flow controller (MFC). The liquid phase is demineralized water with an initial liquid height of 1050 mm and equals about 8.2 L and the working pressure that can be adjusted via the valve at the column top. Experiments were performed for different superficial gas velocities and overpressure in the homogeneous regime.

The probe head (see Fig. 4) has a smaller diameter than the probe body to minimize invasivity. The front of the probe contains the inspection window made of a thermally toughened glass (Metaglas[®], Fa. Huberts Industrieglas) that resists 280°C and 100 bar. The measurement volume is now fixed as no polymer exists allowing a dynamic sealing. Static sealings together with spacers are used for a measurement volume of 12 mm in width.

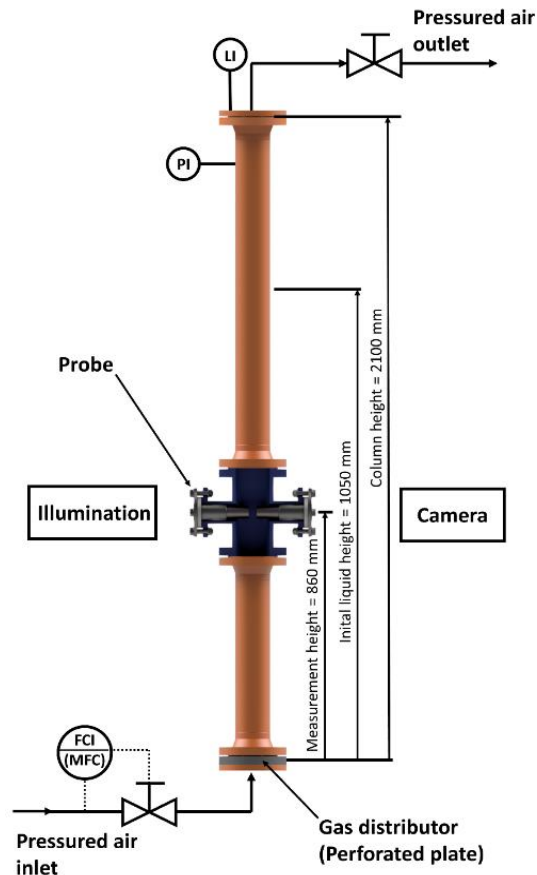


Figure 3. DN100 semi-batch bubble column.

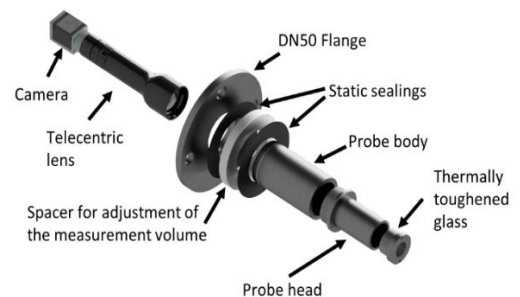


Figure 4. Pressure and temperature stable probe tube with affixed measurement volume.

For the evaluation of the acquired images the following subsequent image algorithm results are given in Fig. 5. The acquired pictures were binarized and the particle areas are blackened with a fill holes

algorithm to prevent segmentation errors in a standard watershed algorithm, where the particles are separated [20].

A size of 1 mm in diameter is the lower threshold for the detection to exclude dust and fragments in the image and additionally a form parameter C_i was used in the range of 0.7 - 1 to exclude non-segmented or erroneous segmented bubbles.

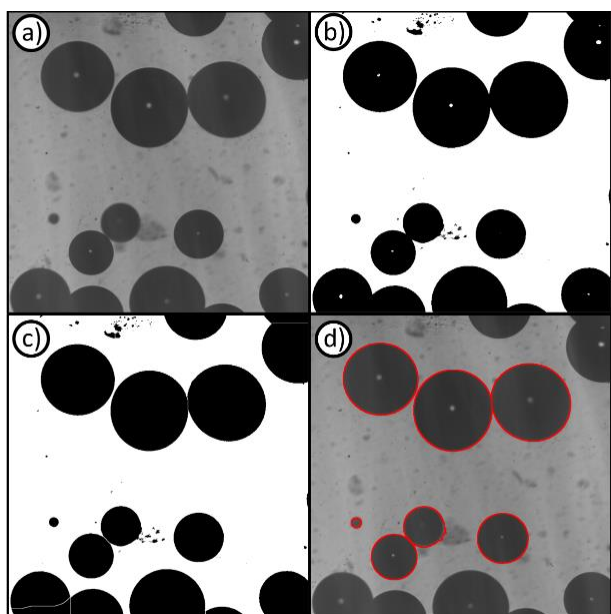


Figure 5. Basic particle detection algorithm based on binary operations. a) original image, b) binary image, c) fill holes and watershed, d) particle detection.

The circularity, C_i , is the roundness of an object and has a value between 0 and 1, where 1 is a perfect circle. It is defined with the perimeter, U , and the area, A :

$$C_i = 4\pi \frac{A}{U^2} \quad (1)$$

As can be seen in Fig. 6, at a superficial gas velocity of $u_g = 2.1$ cm/s an increasing pressure results in a closer BSD with a decreasing mean diameter, as was expected. The mean bubble size decreases from about 5.4 mm at 0 bar pressure to 3.8 mm at 5 bar overpressure in the volume distribution. The pressure difference from 0 bar to 1 bar decreased the bubble mean diameter by 9.2%, from 5.4 mm to 4.9 mm. This shows that even small changes in pressure like the hydrostatic pressure in industrial columns can significantly change the bubble diameter [21].

Crystallizer

The crystal size distribution (CSD) and the final crystal form are decisive for the desired product quality [22] and affect, e. g., the downstream

processing [23, 24] but its determination is still a challenge. In regard to this the shadowgraphic probe was inserted in a 25 L double-jacket draft tube crystallizer with a propeller type stirrer with a diameter of 150 mm stirring at 250 rpm as depicted in Fig. 7. In order to ensure that a similar suspension is measured, the bypass inlet is directly above the probe.

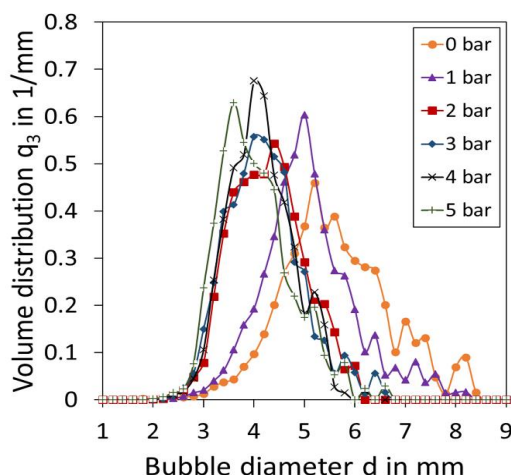


Figure 6. Bubble size distribution; $u_g = 2.1$ cm/s; overpressure between 0 bar and 5 bar.

FTIR was used for concentration measurement and the CSD was detected with a QICPIC online microscope (Fa. Sympatec, Germany) in a bypass and the DN50 shadowgraphic probe (see Fig. 7).

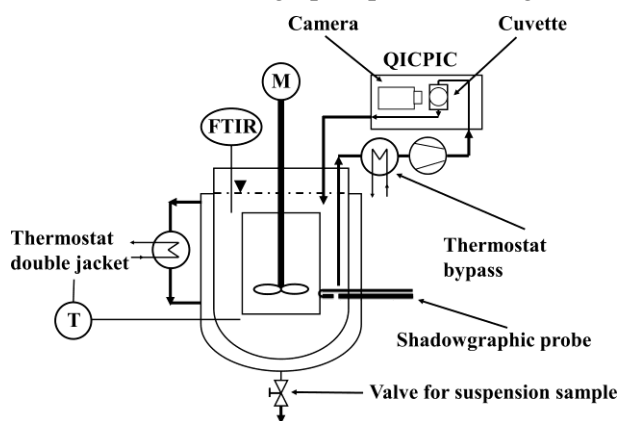


Figure 7. Setup of the 25 L double jacket draft tube crystallizer.

The measurement width in the flow cuvette of the QICPIC and the shadowgraphic probe are both 2 mm. Different experiments were executed in a cooling crystallization with potassium hydrogen phosphate (KH_2PO_4) which was crystallized with seeds from an initial clear aqueous solution. KH_2PO_4 forms resilient bipyramidal crystals, that were already successfully measured with the QICPIC [25, 26]. Suspension samples were taken every 5 min and

at the end of the experiment to have an alternative off-line analysis of the CSD.

Likewise, in Fig. 5 the same procedure in a MATLAB script is used. Binarization with a following background subtraction was used to remove scratches and immobile particles (see Fig. 8b). Morphological closing and fill holes was used to cover the bright areas in the particles and a

segmentation algorithm was not used (see Fig. 8c). Green are detected crystals that fit the form parameters and the red ones are sorted out by the algorithm. The evaluation is based on the body prism width L and a correction factor to consider the rotation of the crystals, as reported elsewhere [27, 28].

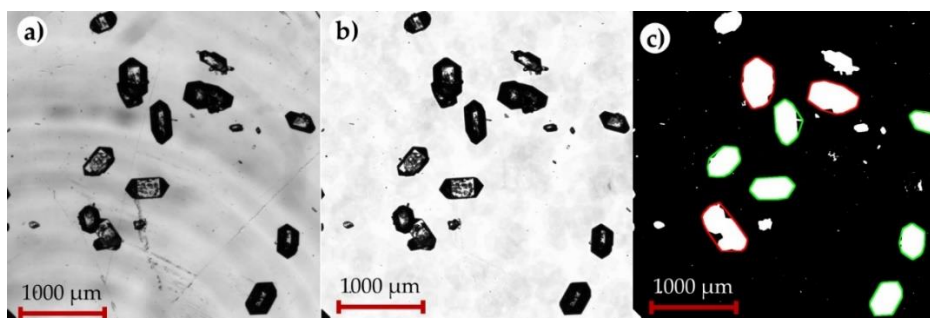


Figure 8. Image processing in MATLAB for crystals. a) original image, b) binary image, c) fill holes and morphological closing with the detection of the convex hull.

In the experiments only single crystals were evaluated, agglomerates and overlapping crystals were excluded. This was realized by using the shape descriptor convexity, C , in a range of 0.95-1 and the eccentricity, ε , between 0.4 and 1. The transient CSD of KH_2PO_4 is here shown exemplarily in Fig. 9 and more details can be found elsewhere [28]. The shadowgraphic probe and the QICPIC that was successfully applied for KH_2PO_4 in the past, gave the same results. Both diagrams show the same start where a bimodal distribution is present, which is conform with the distribution of the added seeds. With increasing experiment time, a larger fraction has grown from about 250 μm up to 280 μm , while the small number of particles increased due to secondary nucleation. These results are additionally verified by sieve analysis, that was taken during the last measurement point at a suspension density of 7 % (see Fig. 10). The sieve analysis confirms the results of the shadowgraphic probe. It was found that this is valid for different temperatures up to 58°C and suspension densities about 12%. It was also found that the shadowgraphic probe has a wider range of operation, as the bypass of the QICPIC tends to blocking, especially at higher temperatures.

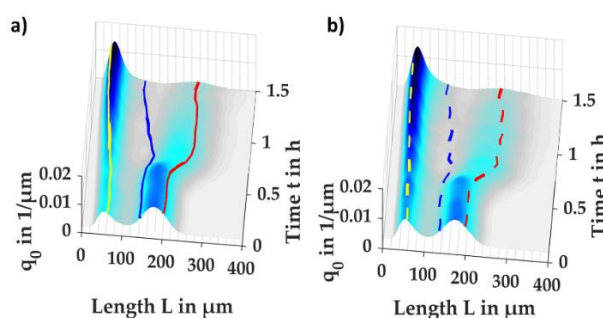


Figure 9. Transient number distribution of a) shadowgraphic probe, b) QICPIC online microscope. The percentiles are shown as following; yellow p_{10} , blue p_{50} and red p_{90} .

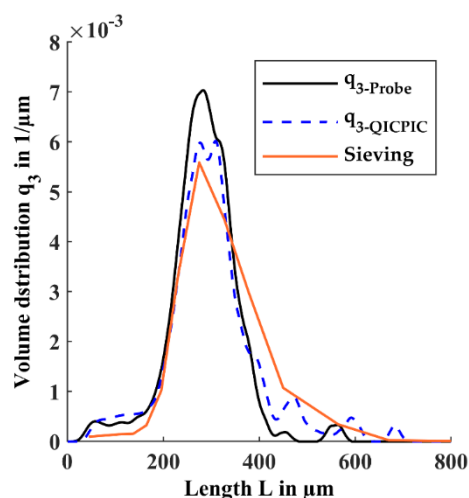


Figure 10. Comparison of the shadowgraphic probe, the online microscope, and the sieve analysis at the end of the experiment.

Pump-mixer

Pump-mixers are continuously operated stirred vessels that are used in mixer-settler cascades in solvent extraction to save pumps [29–31]. The impeller of the vessel is used to mix and pump fluids at the same time. Although these apparatuses are commonly used in industry [32] their scale-up and optimal design is based on rule-of-thumbs. Table 1 gives geometrical details of the DN300 pump-mixer-settler shown in Fig 11.

The liquid feed is controlled by two valves (V1 and V2) and measured by supersonic wave flow indicators (FI), while the two flow rates generate a so-called head Δh in the feed tanks which is

measured *via* a scale. Only V2 is used to adjust the phase ratio in order to maximize the flow rate. To measure the DSD the DN50 endoscopic telecentric probe was used (see Fig. 2b). The probe is inserted from the side *via* a single sided flange at the mixer at the position depicted in Fig. 11. Demineralized water (continuous phase) with 50 mmol/L NaCl guarantees a constant electric conductivity of 8800 $\mu\text{S}/\text{cm}$ and paraffin oil (FC 2006, Fa. Fauth, Germany) is the disperse phase (viscosity of 9.5 mm^2/s , density of 825 kg/m^3). The impeller speed was set to 400 rpm at phase ratios of 10%, 15% and 30%. The DSD is evaluated *via* a modified convolutional neuronal network as reported in [33] exemplarily shown in Fig. 12.

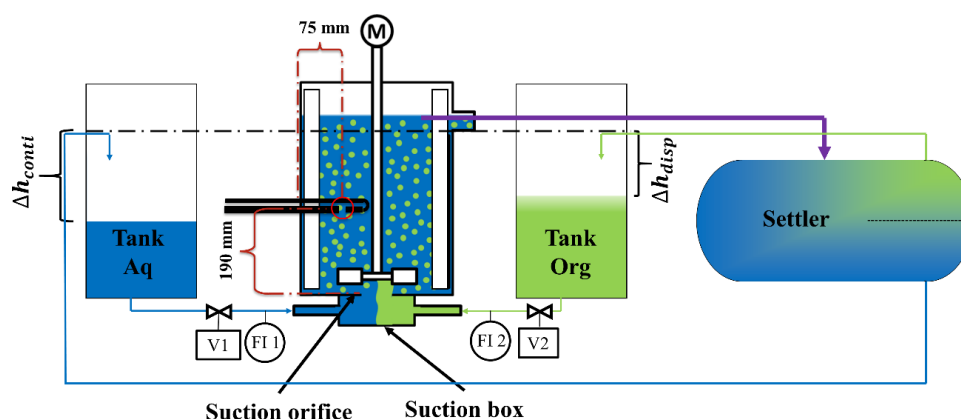


Figure 11. Experimental setup of the DN300 pump-mixer-settler.

Table 1. Pump-mixer dimensions

Tank diameter	T	300 mm
Tank height	H	350 mm
Clearance beneath impeller disc	C	20 mm
Impeller	RT	Rushton turbine (6 blades)
Impeller diameter	D	100 mm (0,3D)
Baffles 4×90°	B	30 mm × 8 mm (width × thickness)
Suction orifice	d	75 mm (0,25T)

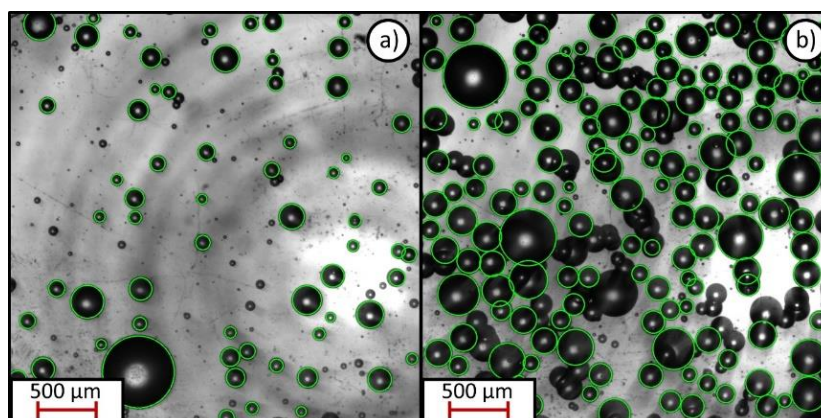


Figure 12. Droplets in the pump-mixer for a) 10% disperse phase, b) 30 % disperse phase.

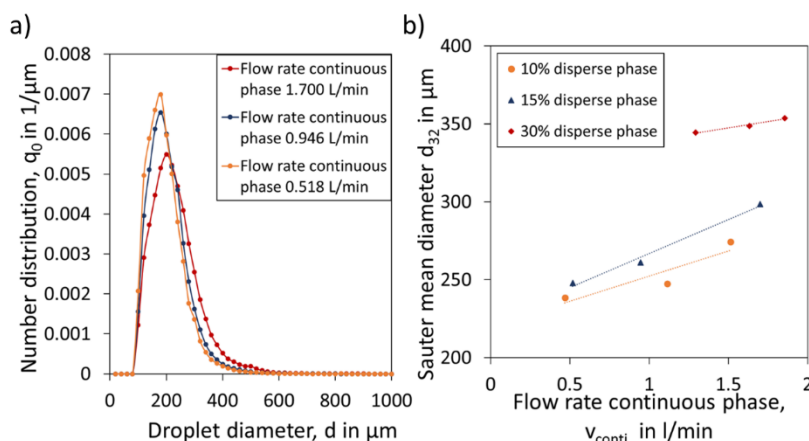


Figure 13. a) DSD for different flow rates at 15% holdup at 400 rpm; b) Sauter mean diameter d_{32} for different phase ratios and flow rates.

The DSD in liquid-liquid dispersions is usually a log-normal-distribution and depends on the flow rate (see Fig. 13a). The impeller produces constant energy dissipation, which leads to droplet breakage. Hence, at low flow rates the energy dissipation per volume of fluid is higher, therefore more droplets break and smaller droplets are produced. On the other hand, higher hold-up leads to more droplet collisions and coalescence, therefore the droplet diameter increases with a higher disperse phase content. As depicted in Fig. 13b, changes in the flow rate at low hold-up lead to significant changes in the Sauter mean diameter, while this effect seems to be less at a higher one. Nevertheless, it could be shown that the shadowgraphic probe can detect even small changes in the DSD. Further on, it was demonstrated that image processing algorithm allows the evaluation of the DSD at industrial relevant disperse phase concentrations up to 30%.

CONCLUSION

The telecentric shadowgraphic probe allows a proper determination of PSD in various apparatuses and processes with an outstanding image quality up to high particle concentrations. Additionally, the telecentric principle provides a constant magnification independent from position, hence, elaborate calibrations or complex image processing algorithms are not needed. It could be shown that this technique can be used for gas-liquid, solid liquid and liquid-liquid systems and can be integrated in different apparatuses with ease, even the applicability for sprays with shadowgraphic methods is reported [34]. The homogeneous bubble column regime and the crystallizer experiments show, that the evaluation of particles can easily be achieved with a simple binary image processing algorithm. This is limited to small disperse phase concentrations (approximately 15 vol.-%), because

the overshadowing of particles leads to erroneous segmentations and therefore false object identifications of the particles. However, the results of the pump-mixer-settler prove that advanced image processing techniques can overcome this drawback and a neuronal network can still properly detect particles at concentrations up to 30 vol. %. In addition, a probe design for the bubble column was presented that allows handling of elevated temperatures and pressures that are omnipresent in industry processes.

This optical inline measurement principle can lead to a better understanding of multiphase flows and helps to reduce the lack of reliable measurement techniques. It was cross-validated with already established measurement techniques, is easy to install and can be used to optimize processes combined with a model predictive control.

Acknowledgement: The authors gratefully acknowledge the Federal Ministry of Education and Research (BMBF) (project “OptiMeOH”) and the German Research Foundation (DFG) (project “Extraktion in Pump-Mischern bei Anwesenheit von Feststoffen, project number: 395373747) for financial support.

REFERENCES

1. M. Lichti, H.-J. Bart, *Chembioeng. Rev.*, **5** (2), 79 (2018).
2. M. Schlüter, *Chem. Ing. Tech.*, **83** (7), 992 (2011).
3. P. Barrett, B. Glennon, *Chem. Eng. Res. Des.*, **80** (7), 799 (2002).
4. A. Amokrane, S. Maaß, F. Lamadie, F. Puel, S. Charton, *Int. J. Chem. Eng.*, **296**, 366 (2016).
5. R. Kopra, H. Mutikainen, O. Dahl, *Tappi J.*, **17** (6), 339 (2018).
6. P. Barrett, B. Glennon, *Part. Part. Syst. Charact.*, **16** (5), 207 (1999).
7. M. Mickler, B. Boecker, H.-J. Bart, *Flow Meas. Instrum.*, **30**, 81 (2013).

8. M. Mickler, H.B. Jildeh, M. Attarakih, H.-J. Bart, *Can. J. Chem. Eng.*, **92** (2), 307 (2014).
9. M. Mickler, H.-J. Bart, *Chem. Ing. Tech.*, **85** (6), 901 (2013).
10. R. Schuhmann, T. Thöniß, *Tech. Mess.*, **65** (4), 131 (1998).
11. S. Maaß, J. Rojahn, R. Hänsch, M. Kraume, *Comput. Chem. Eng.*, **45**, 27 (2012).
12. S. Maaß, S. Wollny, A. Voigt, M. Kraume, *Exp. Fluids*, **50** (2), 259 (2011).
13. J. Schulz, C. Schunk, E. Schleicher, H.-J. Bart, *Chem. Ing. Tech.*, accepted (2020).
14. M. Lichti, H.-J. Bart, C. Roth, EP 3.067.685.A1 (8. Mar.).
15. S. Shu, D. Vidal, F. Bertrand, J. Chaouki, *Renew.*, **141**, 613 (2019).
16. R. Krishna, J. M. van Baten, *Int. Commun. Heat Mass*, **26** (7), 965 (1999).
17. V. V. Buwa, V.V. Ranade, *Chem. Eng. Sci.*, **57** (22-23), 4715 (2002).
18. E. Krepper, B. N. Reddy Vanga, A. Zaruba, H.-M. Prasser, M. A. Lopez de Bertodano, *Nucl. Eng. Des.*, **237** (4), 399 (2007).
19. J. Schäfer, M. W. Hlawitschka, M.M. Attarakih, H.-J. Bart, *AIChE J.*, **65** (10) (2019).
20. M. Lichti, H.-J. Bart, *Flow Meas. Instrum.*, **60**, 164 (2018).
21. P. M. Wilkinson, H. Haringa, L. L. van Dierendonck, *Chem. Eng. Sci.*, **49** (9), 1417 (1994).
22. K. Chow, H. H. Y. Tong, S. Lum, A. H. L. Chow, *J. Pharm. Sci.*, **97** (8), 2855 (2008).
23. C. Wibowo, W.-C. Chang, K.M. Ng, *AIChE J.*, **47** (11), 2474 (2001).
24. R. D. Braatz, *Annu. Rev. Control.*, **26** (1), 87 (2002).
25. H. Eisenschmidt, N. Bajcinca, K. Sundmacher, *Cryst. Growth. Des.*, **16** (6), 3297 (2016).
26. C. Borchert, E. Temmel, H. Eisenschmidt, H. Lorenz, A. Seidel-Morgenstern, K. Sundmacher, *Cryst. Growth. Des.*, **14** (3), 952 (2014).
27. C. Borchert, K. Sundmacher, *Chem. Eng. Technol.*, **34** (4), 545 (2011).
28. D. Wirz, M. Hofmann, H. Lorenz, H.-J. Bart, A. Seidel-Morgenstern, E. Temmel, *Crystals*, **10** (9), 740 (2020).
29. K. K. Singh, K. T. Shenoy, A. K. Mahendra, S. K. Ghosh, *Chem. Eng. Sci.*, **59** (14), 2937 (2004).
30. M. V. Tabib, G. Lane, W. Yang, M. P. Schwarz, *Chem. Eng. Sci.*, **80**, 55 (2012).
31. C. Srilatha, V. V. Morab, T. P. Mundada, A.W. Patwardhan, *Chem. Eng. Sci.*, **65** (11), 3409 (2010).
32. A.T. Davis, T.J. Colven. *AIChE J.*, **7** (1), 72 (1961).
33. J. Schäfer, P. Schmitt, M. W. Hlawitschka, H.-J. Bart, *Chem. Ing. Tech.*, **83** (7), 992 (2019).
34. J. Schulz, H.-J. Bart, *Chem. Eng. Res. Des.*, **147**, 624 (2019).